Simulations of Channel Flows with Effects of Spanwise Rotation or Wall Injection Using a Reynolds Stress Model

Bruno Chaouat*

ONERA , Chatillon 92322, France

Abstract

Simulations of channel flows with effects of spanwise rotation and wall injection are performed using a Reynolds stress model. In this work, the turbulent model is extended for compressible flows and modified for rotation and permeable walls with fluid injection. Comparisons with direct numerical simulations or experimental data are discussed in details for each simulation. For rotating channel flows, the second-order turbulence model yields an asymmetric mean velocity profile as well as turbulent stresses quite close to DNS data. Effects of spanwise rotation near the cyclonic and anticyclonic walls are well observed. For the channel flow with fluid injection through a porous wall, different flows development from laminar to turbulent regime are reproduced. The Reynolds stress model predicts the mean velocity profiles, the transition process and the turbulent stresses in good agreement with experimental data. Effects of turbulence in injected fluid are also investigated.

Introduction

FOR engineering applications, calculations of turbulent flows are generally performed with a first order closure turbulence model based on two transport equations. However, standard two-equation models using the Boussinesq hypothesis have been incapable of accurately predicting flows where the normal Reynolds stresses play an important role, e.g., in flows with strong effects of streamline curvature, system rotation, wall injection or adverse pressure gradient. In turbomachinery, the system rotation affects both mean motion, turbulence intensity and turbulence structure. For instance, due to the Coriolis force, a channel flow subjected to a spanwiswe rotation becomes asymmetric with a turbulence activity which is much reduced to the cyclonic side compared with the anticyclonic side, as

*Senior Scientist, Computational Fluid Dynamics and Aeroacoustics Department.

observed experimentally by Johnson et al.[1] and also reproduced by direct numerical simulations by Kristoffersen and Anderson[2] as well as by Lamballais et al.,[3] more recently. This kind of rotating flow is important for turbomachinery industry. Indeed, in order to improve the performance of jet aircrafts, it is necessary to obtain an accurate description of the flow structure in the different parts of the engine. In solid rocket propulsion,[4] the mass transfer which results from the propellant combustion modifies the shear stress distribution across the flow in comparison with the shear stress of wall-bounded flow. The internal flow in solid rocket motor, which is produced by mass injection, plays an important role in ballistics prediction. Modeling such flows is a difficult task because different regimes from laminar to turbulent can be observed in these motor chambers due to the transition behavior of the mean axial velocity.

The turbulence model used for the closure of the Reynolds averaged Navier-Stokes equations must be able to predict accurately such complex flows. In this aim, Reynolds stress models have been proposed in the past decade. Contrary to first order turbulence models, the Coriolis terms associated with system rotation are included in the second-moment closures. Exact production terms appear as sources (or sinks) in the transport equations for the individual Reynolds stress components. In the RSM formulation, the pressure-strain correlation term forms a pivotal role by incorporating history and non-local effects of the flow. This term has been modeled by assuming homogeneous flows that are near equilibrium[5] and recent developments in this direction have been made.[6] For calculations of complex wall-bounded turbulent flows, a wall reflection term has been incorporated in the model for reproducing the logarithmic region of the turbulent boundary layer.[7] In the usual approach, the modeled wall reflection term requires a variety of *ad hoc* wall damping functions which depend on the distance normal to the wall.[8,9] Durbin[10] has recently proposed an alternative route of a relaxation approach in which an elliptic equation is introduced and interpreted as an approximation of the wall effects. For simulating complex flows, it appears that Reynolds stress models which take into account these recent developments, are a good compromise between large eddy simulations, that require very large computing time, and first order closure models, which are not able to predict flows accurately.

In this work, the model developed by Launder and Shima[11] has been selected because it has predicted flows fairly despite that its formulation is simpler than those of other models.[12] It contains only a few empirical terms and thus is a good candidate to handle a large variety of flows. This model is extended for compressible flows, adapted for rotation and for permeable walls with fluid injection. Comparison with data of direct numerical simulations for non-rotating[13] and rotating[3] channel flows, and with experimental data for channel flows with wall injection,[14] are discussed in details. In addition, the Lumley representation of the second and third invariant of the Reynolds stress anisotropy tensor is considered for analyzing the solutions trajectories.

Governing equations

Turbulent flow of a viscous fluid is considered. As in the usual treatments of turbulence, the flow variable ξ is decomposed into ensemble Reynolds mean and fluctuating parts as $\xi = \overline{\xi} + \xi'$. In the present case, the Favre-averaged is used for compressible fluid so that the variable ξ can be written as $\xi = \tilde{\xi} + \xi''$ with the particular properties $\tilde{\xi''} = 0$ and $\overline{\rho \xi''} = 0$ where ρ is the mass density. These relations imply that $\tilde{\xi} = \overline{\rho\xi}/\bar{\rho}$. The Reynolds average of the Navier-Stokes equations produces in Favre variables the following forms of the mass, momentum and energy equations in a rotation frame of reference Ω :

$$\frac{\partial \bar{\rho}}{\partial t} + \frac{\partial}{\partial x_j}\left(\bar{\rho}\tilde{u}_j\right) = 0 \tag{1}$$

$$\frac{\partial}{\partial t}\left(\bar{\rho}\,\tilde{u}_i\right) + \frac{\partial}{\partial x_j}(\bar{\rho}\,\tilde{u}_i\,\tilde{u}_j) = \frac{\partial \bar{\Sigma}_{ij}}{\partial x_j} - 2\epsilon_{ijk}\bar{\rho}\Omega_j\bar{u}_k \tag{2}$$

$$\begin{aligned} \frac{\partial}{\partial t}(\bar{\rho}\,\tilde{E}) + \frac{\partial}{\partial x_j}(\bar{\rho}\,\tilde{E}\,\tilde{u}_j) &= \frac{\partial}{\partial x_j}\left(\bar{\Sigma}_{ij}\tilde{u}_i\right) \\ +\frac{\partial}{\partial x_j}\left(\overline{\sigma_{ij}u_i''} - \tfrac{1}{2}\bar{\rho}\,\widetilde{u_k''u_k''u_j''}\right) &- \frac{\partial \bar{q}_j}{\partial x_j} \end{aligned} \tag{3}$$

where u_i, E, Σ_{ij}, σ_{ij}, q_i, ϵ_{ijk} are, respectively, the velocity vector, the total energy, the total stress tensor, the viscous stress tensor, the total heat flux vector and the permutation tensor. The mean stress tensor $\bar{\Sigma}_{ij}$ is composed by the mean modified pressure which includes the centrifugal force potential $\bar{p^*} = \bar{p} - \frac{1}{2}\bar{\rho}|\Omega \times \mathbf{x}|^2$, the mean viscous stress $\bar{\sigma}_{ij}$ and the turbulent stress $\bar{\rho}\,\tau_{ij}$ as follows :

$$\bar{\Sigma}_{ij} = -\bar{p^*}\,\delta_{ij} + \bar{\sigma}_{ij} - \bar{\rho}\,\tau_{ij} \tag{4}$$

In this expression, the tensor $\bar{\sigma}_{ij}$ takes the usual form :

$$\bar{\sigma}_{ij} = \bar{\mu}\left(\frac{\partial \bar{u}_i}{\partial x_j} + \frac{\partial \bar{u}_j}{\partial x_i}\right) - \frac{2}{3}\bar{\mu}\frac{\partial \bar{u}_k}{\partial x_k}\delta_{ij} \tag{5}$$

and the Favre-averaged Reynolds stress tensor is :

$$\tau_{ij} = \widetilde{u_i'' u_j''} \tag{6}$$

where the quantity μ is the molecular viscosity. The mean heat flux $\bar{q}_i$ is composed by the laminar and turbulent flux contributions :

$$\bar{q}_i = -\kappa \frac{\partial \bar{T}}{\partial x_i} + \bar{\rho}\, \widetilde{h'' u_i''} \tag{7}$$

where T, h and κ are the temperature, the specific enthalpy and the thermal conductivity, respectively. Closure of the mean flow equations is necessary for the turbulent stress $\bar{\rho}\, \widetilde{u_i'' u_j''}$, the molecular diffusion $\overline{\sigma_{ij} u_i''}$, the turbulent transport of the turbulent kinetic energy $\bar{\rho}\, \widetilde{u_k'' u_k'' u_j''}$, and the turbulent heat flux $\bar{\rho}\, \widetilde{h'' u_i''}$.

Turbulence model

The Favre-averaged correlation tensor $\tau_{ij} = \widetilde{u_i'' u_j''}$ is computed by means of Reynolds stress model. In this study, the model of Launder and Shima[11] has been considered and extended to compressible flows using the Favre-averaged. The turbulent model has been also modified to simulate rotating flows. For this, the Coriolis force has been incorporated in the Reynolds stress transport equation and the pressure-strain correlation has been developed in a form-invariant under Galilean transformation. This has consisted in replacing the mean vorticity tensor $\bar{\omega}_{ij}$ of usual form,

$$\bar{\omega}_{ij} = \frac{1}{2}\left(\frac{\partial \bar{u}_i}{\partial x_j} - \frac{\partial \bar{u}_j}{\partial x_i} \right) \tag{8}$$

which appears in the modeled pressure-strain term, by the absolute mean vorticity tensor defined as $\bar{W}_{ij} = \bar{\omega}_{ij} + \epsilon_{mji}\Omega_m$, where Ω is the angular velocity vector. So that the pressure-strain term takes the following form :

$$\begin{aligned} \Phi_{ij} &= -c_1 \bar{\rho} \epsilon a_{ij} + \tfrac{4}{3} c_2 \bar{\rho} k \bar{S}_{ij} \\ &+ c_2 \bar{\rho} k \left(a_{ik} \bar{S}_{jk} + a_{jk} \bar{S}_{ik} - \tfrac{2}{3} a_{mn} \bar{S}_{mn} \delta_{ij} \right) \\ &+ c_2 \bar{\rho} k \left(a_{ik} \bar{W}_{jk} + a_{jk} \bar{W}_{ik} \right) \end{aligned} \tag{9}$$

where k is the turbulent kinetic energy, $a_{ij} = (\tau_{ij} - \frac{2}{3}k\delta_{ij})/k$ is the anisotropic tensor, $\bar{S}_{ij}$ is the mean rate of strain defined as :

$$\bar{S}_{ij} = \frac{1}{2}\left(\frac{\partial \bar{u}_i}{\partial x_j} + \frac{\partial \bar{u}_j}{\partial x_i}\right) \tag{10}$$

ϵ is the dissipation rate and c_1 and c_2 are functions dependant of the second and third invariants $A_2 = a_{ij}a_{ji}$, $A_3 = a_{ij}a_{jk}a_{ki}$. Then, equation (9) is rewritten with respect to the Reynolds stress τ_{ij} and the mean velocity gradient $\partial \bar{u}_i/\partial x_j$ in order to obtain a more compact form for the slow and rapid contributions, Φ^1_{ij}, Φ^2_{ij} of the pressure-strain correlations[15] such as $\Phi_{ij} = \Phi^1_{ij} + \Phi^2_{ij}$. Expressions of these quantities are the following :

$$\Phi^1_{ij} = -c_1\bar{\rho}\epsilon a_{ij} \tag{11}$$

$$\Phi^2_{ij} = -c_2\left(P_{ij} + \tfrac{1}{2}P^R_{ij} - \tfrac{1}{3}P_{kk}\delta_{ij}\right) \tag{12}$$

where P_{ij} is the production by the mean flow :

$$P_{ij} = -\bar{\rho}\tau_{ik}\frac{\partial \tilde{u}_j}{\partial x_k} - \bar{\rho}\tau_{jk}\frac{\partial \tilde{u}_i}{\partial x_k} \tag{13}$$

and P^R_{ij} is the production generated by the rotation :

$$P^R_{ij} = -2\bar{\rho}\Omega_p\left(\epsilon_{jpk}\tau_{ki} + \epsilon_{ipk}\tau_{kj}\right) \tag{14}$$

Due to these considerations, the modeled transport equation of the Reynolds stress tensor takes the form as follows :

$$\begin{aligned}\frac{\partial}{\partial t}(\bar{\rho}\,\tau_{ij}) + \frac{\partial}{\partial x_k}(\bar{\rho}\,\tau_{ij}\tilde{u}_k) = P_{ij} + P^R_{ij} \\ -\frac{2}{3}\bar{\rho}\epsilon\delta_{ij} + \Phi^1_{ij} + \Phi^2_{ij} + \Phi^w_{ij} + J_{ijk}\end{aligned} \tag{15}$$

where :

$$\begin{aligned}\Phi^w_{ij} = c^w_1\frac{\bar{\rho}\epsilon}{k}\left(\tau_{kl}n_kn_l\delta_{ij} - \tfrac{3}{2}\tau_{ki}n_kn_j - \tfrac{3}{2}\tau_{kj}n_kn_i\right)f_w \\ +c^w_2(\Phi^2_{kl}n_kn_l\delta_{ij} - \tfrac{3}{2}\Phi^2_{ik}n_kn_j - \tfrac{3}{2}\Phi^2_{jk}n_kn_i)f_w\end{aligned} \tag{16}$$

$$J_{ijk} = \frac{\partial}{\partial x_k}\left(\bar{\mu}\frac{\partial \tau_{ij}}{\partial x_k} + c_s\bar{\rho}\frac{k}{\epsilon}\tau_{kl}\frac{\partial \tau_{ij}}{\partial x_l}\right) \tag{17}$$

The terms on the right-hand side of equation (15) are identified as production by the mean flow, dissipation rate, slow redistribution, rapid redistribution, wall reflection and diffusion. The wall reflection term has been introduced in the model in order to take into account the pressure fluctuations from a rigid wall. The functions c_1, c_2, c_1^w, c_2^w are empirically calibrated as : $c_1 = 1 + 2.58AA_2^{1/4}(1-\exp(-(0.0067R_t)^2))$, $c_2 = 0.75A^{1/2}$, $c_1^w = -\frac{2}{3}c_1 + 1.67$, $c_2^w = \max(\frac{2}{3}c_2 - \frac{1}{6}, 0)/c_2$ where $A = 1 - 9/8(A_2 - A_3)$ is the flatness coefficient parameter and $R_t = k^2/\nu\epsilon$ is the turbulent Reynolds number. In expression (16), $f_w = 0.4k^{\frac{3}{2}}/\epsilon x_n$ is a function dependant of the normal distance to the wall x_n and n is the normal to the wall. The coefficiant c_s takes the value of 0.22. The dissipation rate ϵ of expression (15) is computed by means of the following transport equation which takes the form as :

$$\frac{\partial}{\partial t}(\bar{\rho}\epsilon) + \frac{\partial}{\partial x_j}(\bar{\rho}\tilde{u}_j\epsilon) = \frac{\partial}{\partial x_j}\left(\bar{\mu}\frac{\partial \epsilon}{\partial x_j} + c_\epsilon\bar{\rho}\frac{k}{\epsilon}\tau_{jl}\frac{\partial \epsilon}{\partial x_l}\right)$$
$$-\left(c_{\epsilon 1} + \psi_1 + \psi_2\right)\bar{\rho}\frac{\epsilon}{k}\tau_{ij}\frac{\partial \tilde{u}_j}{\partial x_i} - c_{\epsilon 2}\bar{\rho}\frac{\tilde{\epsilon}\epsilon}{k} \tag{18}$$

with $c_{\epsilon 1} = 1.45$, $c_{\epsilon 2} = 1.9$, $c_\epsilon = 0.18$ where

$$\tilde{\epsilon} = \epsilon - 2\nu\left(\frac{\partial\sqrt{k}}{\partial x_n}\right)^2 \tag{19}$$

The function ψ_1 in equation (18) is defined as :

$$\psi_1 = 1.5A\left(\frac{P_{ii}}{2\bar{\rho}\,\epsilon} - 1\right) \tag{20}$$

and has the effect to reduce the turbulence length scale. Relative to the model of Shima,[16] the function ψ_1 has been modified to simulate flows with fluid injection through a porous wall. The reason is that this function can reach too large values, in comparison with the standard value $c_{\epsilon 1}$, when flows are far from equilibrium. Due to these considerations, the function ψ_1 has been bounded, $|\psi_1| < 0.125\,c_{\epsilon 1}$. This has the effects to prevent too early laminarization of flows. On the other hand, the function ψ_2 has been reduced to zero because of its empirical character which alters the rationale formulation of the dissipation rate equation.

Regarding to the molecular diffusion and the turbulent transport terms, a gradient hypothesis has been considered :

$$\overline{\sigma_{ij} u_i''} - \frac{1}{2}\bar{\rho}\, \widetilde{u_k'' u_k'' u_j''} = \left(\bar{\mu} + c_s \bar{\rho} \frac{k}{\epsilon} \tau_{jk}\right) \frac{\partial k}{\partial x_j} \tag{21}$$

For the heat transfer, the turbulent flux is computed by means of the k and ϵ variables :

$$\widetilde{h'' u_i''} = -\frac{c_\mu k^2}{\epsilon} \frac{c_p}{P_{r_t}} \frac{\partial \bar{T}}{\partial x_i} \tag{22}$$

where c_p and P_{r_t} are the specific heat at constant pressure and the turbulent Prandtl number, respectively. The coefficiant c_μ takes the standard value 0.09.

Realizability conditions for the RSM model

The Reynolds stress tensor τ_{ij} computed by the modeled transport equation (15) must satisfy the realizability conditions which imply non-negative values of the three principal invariants[17] I_i that appear in the characteristic polynomial $P(\lambda) = \lambda^3 - I_1\lambda^2 + I_2\lambda - I_3$ of the matrix formed by the components τ_{ij}. It is easier to examine the question of realizability in a coordinate system aligned with the principal axes of the Reynolds stress tensor. For practical reasons, it is also more convenient to analyze the weak form of realizability[17] which requires that when a principal Reynolds stress componant vanishes, its time derivative must be positive. This ensures that negative energy component cannot occur when this constraint is satisfied. Although the basis of the principal axes of the Reynolds stress tensor is rotating in time, Speziale et *al.*[18] have shown that the first derivative constraint takes the same formulation in the principal axes. So that the modeled transport equation (15) of the turbulent stress componant $\tau_{(\alpha\alpha)}$ can be written as :

$$\begin{aligned} \bar{\rho}\frac{d\tau_{(\alpha\alpha)}}{dt} &= P_{(\alpha\alpha)} + P^R_{(\alpha\alpha)} - \tfrac{2}{3}\bar{\rho}\epsilon - c_1\bar{\rho}\frac{\epsilon}{k}(\tau_{(\alpha\alpha)} - \tfrac{2}{3}k) \\ &- c_2(P_{(\alpha\alpha)} + \tfrac{1}{2}P^R_{(\alpha\alpha)} - \tfrac{1}{3}P_{\alpha\alpha}) \end{aligned} \tag{23}$$

where the Einstein summation convention is suspended for indices which lies within parentheses. The diffusion term as well as the reflection term are not considered. When the componant stress $\tau_{(\alpha\alpha)}$ vanishes, it can be shown that the production terms $P_{(\alpha\alpha)}$ and $P^R_{(\alpha\alpha)}$ are zero so that the weak realisability conditions implies :

$$c_1 \geq 1 - c_2 \frac{P_{\alpha\alpha}}{2\bar{\rho}\epsilon} \tag{24}$$

Due to the expressions of the coefficients c_1 and c_2, equation (24) is verified when the production term $P_{\alpha\alpha}$ of the turbulent kinetic energy is positive. This corresponds to the usual case of flow physics and ensures therefore the satisfaction of the weak realizability constraint.

Non-rotating channel flow

Numerical simulation of fully developed turbulent channel flow is compared with data of direct numerical simulation[13] for the Reynolds number $R_\tau = u_\tau \delta/2\nu = 395$, based on the averaged friction velocity u_τ and the channel width $\delta/2$, (see figure 1 with $\Omega = 0$). Other useful definitions of the Reynolds number include those based on the mean centerline velocity $R_c = u_c\delta/\nu$ and the bulk velocity $R_m = u_m\delta/\nu$. In the present case, RSM results can be compared with DNS data computed for incompressible flow because the Mach number takes a low value. The closure equation (22) hasn't influenced the numerical results due to the fact that the temperature is almost uniform. Figure 2 (a) describes the dimensionless velocity profile $\bar{u}_1/u_\tau$ in wall coordinates $x_2^+ = x_2 u_\tau/\nu$ in order to illustrate the logarithmic region. The velocity follows very well the DNS data but the logarithmic profile is not completely resolved in the center of the channel. The ratio of the centerline velocity to the bulk velocity takes the value 1.13, quite close to DNS result, 1.15. Excellent agreement with Dean's correlation of $u_c/u_m = 1.28 R_m^{-0.0116} = 1.15$ is also obtained. The value of the skin friction coefficient computed by Dean's suggested correlation $c_f = 0.073 R_m^{-0.25} = 6.80$ agrees well the DNS result, 6.70. Figures 2 (b) shows the axial, normal and spanwise turbulence intensities normalized by the wall-shear velocity $(\widetilde{u_i'' u_i''})^{1/2}/u_\tau$ (i=1,2,3), versus the global coordinates x_2/δ. The Reynolds stress model provides good agreement with the DNS data. In particular, the peak of the streamwise turbulence intensity in the wall region is well captured.

Rotating channel flows

Numerical simulations of rotating channel flows are performed for the Reynolds number $R_\tau = 162$, based on the friction velocity u_τ which is defined as $u_\tau = \sqrt{\frac{1}{2}(u_{\tau c}^2 + u_{\tau a}^2)}$ where $u_{\tau c}$ and $u_{\tau a}$ are respectively the friction velocities on the cyclonic and anticyclonic walls. The Reynolds number based on the bulk velocity takes the value $R_m = 5000$. For this application, different values of the Rossby number $R_o = 3u_m/\delta\Omega$ are considered, $R_o = 18$ and $R_o = 6$, respectively. These values correspond to moderate and high rotation regimes. The vector rotation considered is along the spanwise direction x_3 as indicated in figure 1. Figures 3 (a), (b) show the mean dimensionless velocity profiles normalized by the bulk velocity $\bar{u}_1/u_m$ versus the global coordinates for both rotation regimes. These figures illustrate the asymmetric character of the flow because of the rotation effects. For both rotation regimes, an excellent agreement between the RSM simulations and DNS data of Lamballais et *al.*[3] is observed. For these rotating flows, it is of interest to note that the mean component $\bar{u}_1$ of the velocity is only affected by the Coriolis term through the turbulent shear stress τ_{12} which appears in the momentum equation (2). For $k-\epsilon$ model with a Boussinesq hypothesis, it is a simple matter to show that the mean velocity profile remains perfectly symmetric. For both simulations performed at $R_o = 18$ and $R_o = 6$, one can notice that the mean velocity profile exhibits a linear region of constant shear stress. The computation indicates that the slope of the mean velocity gradient $\partial \bar{u}_1/\partial x_2$ is approximately equal to $2\Omega_3$, and corresponds to a nearly-zero mean spanwise absolute vorticity vector, i.e., $\bar{W}_3 = \bar{\omega}_3 + 2\Omega_3 \approx 0$ where $\omega_i = \epsilon_{ijk}\partial u_k/\partial x_j$ represents the vorticity vector, as already noticed experimentally by Johnston et *al.*[1] By considering the Richardson number defined as :

$$R_i = \frac{-\Omega_3(S_{12} - \Omega_3)}{S_{12}^2} \tag{25}$$

it can be mentioned that this particular portion of the profile represents a region of neutral stability $R_i \approx 0$. On the cyclonic side, the flow is stabilized since the Richardson number R_i is positive wheras negative values on the anticyclonic wall imply that the rotation destabilizes the flow.[19] Figures 3 (c),(d) show the evolutions of the axial, normal and spanwise turbulence intensities normalized by the bulk velocity $(\widetilde{u_i'' u_i''})^{1/2}/u_m$ (i=1,2,3) versus the global coordinates x_2/δ for both rotation regimes. The model predicts Reynolds turbulent stresses in excellent agreement with DNS data[3] for the moderate rotation regime $R_o = 18$. For the higher rotation $R_o = 6$, a very good agreement is also observed with the DNS data although that the turbulence intensity is slightly overpredicted in the cyclonic wall region. The distribution of the turbulence fluctuations differs appreciably in the non-rotating and rotating cases. When the rotation rate is increased, the turbulence activity is much more reduced for the cyclonic wall than for the anticyclonic wall. This suggests that the turbulence on the cyclonic side may originate from interaction with turbulent anticyclonic side. Due to the rotation, the flow anisotropy is modified. Near the anticyclonic side, the intensity of the streamwise velocity fluctuations $(\widetilde{u_1'' u_1''})^{1/2}/u_m$ decreases with the rotation rate wheras the intensities of the normal and spanwise velocity fluctuations $(\widetilde{u_2'' u_2''})^{1/2}/u_m$, $(\widetilde{u_3'' u_3''})^{1/2}/u_m$ are increased. On the other hand, it can be observed a monotonic decrease of the root-mean square velocity components $(\widetilde{u_i'' u_i''})^{1/2}/u_m$ (i=1,2,3) near the cyclonic channel side. Figures 3 (e),(f) show the Reynolds shear stress normalized by the bulk velocity $\widetilde{u_1'' u_2''}\ /u_m^2$ in global coordinates for both Rossby numbers. The asymmetric character of the flow is well illustrated. Figure 4 describes the evolution of the normalized friction velocities on the cyclonic and anticyclonic walls u_τ/u_* versus the number rotation $R_{ot} = \Omega\delta/u_m = 3/R_o$. The quantity

u_* is the friction velocity in the absence of rotation. The present results produced by the Reynolds stress model appear to be quite close to DNS data of Kristoffersen and Andersson[2] but slightly overpredicted near the anticyclonic wall in comparison with data of Lamballais et al.[3] Figure 5 shows the solution trajectories projected onto the plane formed by the second invariant and third invariant for the DNS simulation and RSM prediction. The solution trajectories are computed along a straight line normal to the walls in a cross section of the channel. It can be seen that the trajectories produced by the model remain inside the curvilinear triangle which is the realizable region, and agree well with the DNS trajectories. Due to rotation, the trajectories are not symmetric when moving from the anticyclonic wall toward the cyclonic wall.

Channel flows with wall injection

The objective is to investigate the flow in a channel with appreciable fluid injection through a permeable wall as indicated in figure 6. The wall injection is encountered in the combustion induced flowfields in solid propellant rocket motors (SRM). It is known that the flow in a channel with wall injection evolves significantly with respect to the distance from the front wall. Different regimes of flow are observed depending on the injection Reynolds number $R_s = \rho_s u_s \delta/\mu$, defined with the injection density ρ_s, the velocity u_s, the dynamics viscosity μ, at the porous surface and with the height δ of the planar channel. In the first regime, the velocity field is developed in accordance with the laminar theory. The second flow regime is characterized by the development of turbulence and is affected by the transition process of the mean axial velocity when a critical turbulence threshold is attained. Simulations of channel flows with wall injection using a first order closure model have provided different predictions of the transition process and overpredicted turbulence levels by about 300% and 200% in the post-transition of the flow.[20–22] Simulations using a second order closure model with an algebraic relation for the turbulence macro-length scale were performed by Beddini.[23] Experimental data of Yamada et al.[24] were overpredicted by about 200 % but a reasonable agreement with the data of Dunlap et al.[25] was obtained by generating pseudo-turbulence at the porous surface. These previous numerical results show that channel flows with wall injection present physics phenomena that are difficult to reproduce by simulations. A recent specific experimental set up has been realized at ONERA for investigating the characterictics of injection driven flows. The planar experimental facility is composed of a parallelepipedic channel bounded by a lower porous plate. Values of the duct length and the channel height are respectively $L = 58.1$ cm and $\delta = 1.03$ cm. Cold air at 303 K is injected with a uniform mass flow rate $m = 2.619\ Kg/m^2s$ through a porous material of porosities, 8 μm or 18 μm. The injection velocities are fixed by the local pressure in the channel. In accordance with the operating conditions of the experimental set up, the pressure at the head-end of the channel is $p_o = 1.5$ bar wheras the exit pressure is $p_e = 1.374$ bar. Due to the mass conservation equation, the flow Reynolds number $R_m = \rho_m u_m \delta/\mu$ based on the bulk density ρ_m and the bulk velocity u_m varies linearly versus the axial distance of the channel so that it can be computed as $R_m = m x_1/\mu$. It ranges from zero to the approximately value 9 x 10^4. The injection Reynolds number is close to 1600. Experiments have been carried out by Avalon.[14]

Different boundary conditions are applied in the computational domain. For the impermeable walls, no slip on velocity and constant temperature are required. Zero turbulent kinetic energy and the wall dissipation rate value $\epsilon_w = 2\nu(\partial\sqrt{k}/\partial x_n)^2$ are specified. For the permeable wall, the inflow boundary condition requires a constant mass flow rate at the same temperature. Experimental investigations[14,26] of injected air from porous plate indicate that some stationary velocity fluctuations appear in the flow and that the disturbance amplitude increases with increasing injection velocity. Due to this situation, the turbulence fluctuations at the porous surface can be related to the mean injected velocity by means of a coefficient defined as $\sigma_s = (\widetilde{u_2''u_2''/u_s^2})^{1/2}$ to be parametrically investigated. Other correlations such as $\widetilde{u_1''u_1''}$ or $\widetilde{u_3''u_3''}$ are smaller than the normal velocity fluctuations $\widetilde{u_2''u_2''}$ of the injected flow. In this work, several simulations are performed for investigating the influence of turbulence in injected fluid, $\sigma_s = 0.1$, 0.2, 0.3, 0.4 and 0.5. For injection of low turbulence intensity, the reasonable wall dissipation ϵ_w is also imposed at the porous surface. An other point to emphazise concerns the pressure fluctuations. Considering that the permeable wall does not reflect the pressure fluctuations, the term Φ_{ij}^w of equation (15) is reduced to zero in the normal direction to the permeable wall. The slow and rapid pressure-strain correlation terms Φ_{ij}^1 and Φ_{ij}^2 of equations (11) and (12) have not be modified. The reason is that the functions c_1 and c_2 in that modeled terms are dependant of the flow turbulent variables, such as the anisotropy tensor a_{ij} or the Reynolds number R_t, and are automatically modified by the nature of the flow. No more modifications are necessary because the local effects of flowfield anisotropy near wall are incorporated in the modeled term[11] $\Phi_{ij} - \frac{2}{3}\bar{\rho}\epsilon\delta_{ij}$.

Figure 7 (a) shows the streamlines and the mean velocities of the flowfield. Strong effects of the streamlines curvature are observed near the porous wall due to the fluid injection. The velocities increase rapidly in the boundary layer generated by the rigid wall. Figure 7 (b) illustrates the Mach number contours of the channel flow. High resolution of the steady state computational flowfield can be observed through the regular behavior of the contour lines. The Mach number ranges from zero in the head-end of the channel to approximately 0.33 in the exit section.

Several simulations have been performed to investigate the influence of the turbulence injection. As it could be expected, the turbulence transition is affected by the pseudo-turbulence injected through the porous wall. Figures 7 (c),(d) show the contours of the turbulent Reynolds number $R_t = k^2/\nu\epsilon$ for different values of the injection parameter. The turbulence is first developed in the impermeable wall region and afterwise in the permeable wall region. Increasing of pseudo-turbulence intensity can anticipate the flow transition near the permeable wall but has no effect on the flow in the impermeable wall region. Figure 8 (a) shows the evolution of the Reynolds number $R_\tau = u_\tau \delta/2\nu$ based on the averaged friction velocity u_τ versus the longitudinal distance of the channel. The averaged friction velocity is defined as $u_\tau = \sqrt{\frac{1}{2}(u_{\tau w}^2 + u_{\tau m}^2)}$ where $u_{\tau w}$ and $u_{\tau m}$ are the friction velocities computed on the impermeable and permeable walls, respectively. The rapid rise of the Reynolds number which occurs in the first part of the channel at 0.2 m corresponds to the flow transition near the impermeable wall region. Figure 8 (b) shows the evolutions of the integral turbulent coefficient

$$\alpha = \frac{c_\mu}{\mu\delta}\int_0^\delta \frac{\bar{\rho}k^2}{\epsilon} dx_2 \tag{26}$$

for different values of the injection paramater σ_s. The rises of the coefficient α figure out the transition locations of the turbulent flow. It can be noticed that the low initial turbulence injection for $\sigma_s = 0.1$ is too small to triger the transition regime. It appears that the flow turbulence intensity remains insensitive to the injected turbulence level when such level is large. Figure 9 (a) shows the dimensionless mean velocity profiles normalized by the bulk velocity $\bar{u}_1/u_m$ in global coordinates x_2/δ for $\sigma_s = 0.2$. The general shapes of the profiles present a good agreement with experimental data. The flatness of the curves is attributed to the turbulent effects which increase when moving to the exit section of the channel. Figures 9 (b),(c),(d) show the evolutions of the streamwise, normal and cross turbulent velocity fluctuations normalized by the bulk velocity, $(\widetilde{u_1''u_1''})^{1/2}/u_m$, $(\widetilde{u_2''u_2''})^{1/2}/u_m$, $(\widetilde{u_1''u_2''})/u_m^2$, for $\sigma_s = 0.2$ in different sections of the channel located at $x_1 = 22$ cm, 40 cm and 57 cm. In general way, it can be observed that the levels of the Reynolds stresses of the flow are fairly reproduced by the RSM model although that a minor discrepancie with the experimental data appears for the last section. The disagreement near the impermeable side must be attributed to the experimental data which are altered by the hot wire probe which is introduced through the impermeable wall. Figures 10 (a), (b) show the normal velocity fluctuations $(\widetilde{u_2''u_2''})^{1/2}/u_m$, in different cross sections for the RSM and the $k-\epsilon$ model of Myong and Kasagi.[27] The $k-\epsilon$ model overpredicts the turbulent stresses by about 300 %.

Conclusion

Numerical flow field simulations for the non-rotating fully developed channel flow, the rotating channel flows and the channel flows with wall injection have been performed using a Reynolds stress model. Comprehensive comparisons with DNS data or experimental data for each encountered configuration have been presented. It has been demonstrated that the model which has been extended for compressible flows and modified for system rotation and wall injection predicts accurately the flows. For rotating channel flows, the RSM model yields asymmetric mean velocity and turbulent stresses in very good agreement with the DNS data. For the channel flow with fluid injection through a permeable wall, different flow regimes from laminar to turbulent as well as the transition of the mean velocity profile, have been reproduced in accordance with the experimental data. Because of the presence of permeable and impermeable walls, the development of turbulence occurs at two different locations in the channel. Effects of pseudo-turbulence in injected fluid through the porous surface have also been investigated.

References

[1]Johnston, J. P., Halleen, R. M., and Lezius, D. K., "Effects of Spanwise Rotation on the Structure of Two-Dimensional Fully Developed Turbulent Channel Flow," *Journal of Fluid Mechanics*, Vol. 56, 1972, pp. 533–557.

[2]Kristoffersen, R. and Andersson, H. I., "Direct simulations of low-Reynolds-number turbulent flow in a rotating channel," *Journal of Fluid Mechanics*, Vol. 256, 1993, pp. 163–197.

[3]Lamballais, E., Métais, O., and Lesieur, M., "Spectral-Dynamic Model for Large-Eddy Simulations of Turbulent Rotating Flow," *Theoret. Comput. Fluid Dynamics*, Vol. 12, 1998, pp. 149–177.

[4]Chaouat, B., "Flow Analysis of a Solid Propellant Rocket Motor with Aft Fins," *Journal of Propulsion and Power*, Vol. 13, No. 2, 1997, pp. 194–196.

[5]Launder, B. E., Reece, G. J., and Rodi, W., "Progress in the Development of a Reynolds Stress Turbulence Closure," *Journal of Fluid Mechanics*, Vol. 68, 1975, pp. 537–566.

[6]Speziale, C. G., Sarkar, S., and Gatski, T. B., "Modelling the Pressure-Strain Correlation of Turbulence: an Invariant Dynamical Systems Approach," *Journal of Fluid Mechanics*, Vol. 227, 1991, pp. 245–272.

[7]Gibson, M. M. and Launder, B. E., "Ground effects on pressure fluctuations in the atmospheric boundary layer," *Journal of Fluid Mechanics*, Vol. 86, 1978, pp. 491–511.

[8]So, R. M., Lai, Y. G., and Zhang, H. S., "Second Order Near Wall Turbulence Closures: a Review," *AIAA Journal*, Vol. 29, No. 11, 1991, pp. 1819–1835.

[9]K. Hanjalic, I. Hadzic, S. J., "Modeling Turbulent Wall Flows Sunjected to Strong Pressure Variations," *Journal of Fluid Engineering*, Vol. 121, 1999, pp. 57–64.

[10]Durbin, P. A., "A Reynolds Stress Model for Near-Wall Turbulence," *Journal of Fluid Mechanics*, Vol. 249, 1993, pp. 465–498.

[11]Launder, B. E. and Shima, N., "Second Moment Closure for the Near Wall Sublayer: Development and Application," *AIAA Journal*, Vol. 27, No. 10, 1989, pp. 1319–1325.

[12]Pettersson, B. A. and Andersson, H. I., "Near Wall Reynolds Stress Modelling in Noninertial Frames of Reference," *Fluid Dynamic Research*, Vol. 19, 1997, pp. 251–276.

[13]Moser, R., Kim, D., and Mansour, N., "Direct Numerical Simulation of Turbulent Channel Flow up to $R_\tau = 590$," *Physics of Fluid*, Vol. 11, No. 4, 1999, pp. 943–945.

[14]Avalon, G., "Flow Instabilities and Acoustic Resonance of Channels with Wall Injection," AIAA Paper 98–3218, Jul. 1998, In 34th AIAA/ASME/SAE/ASEE Joint Propulsion Conference and Exhibit.

[15]Chaouat, B., "Numerical Simulations of Fully Developed Channel Flows Using k-ϵ, Algebraic and Reynolds Stress Models," AIAA Paper 99–0158, Jan. 1999, In 37th AIAA Aerospace Sciences Meeting and Exhibit.

[16]Shima, N., "Prediction of Turbulent Boundary Layers with a Second-moment Closure: Part I - Effects of Periodic Presure Gradient, Wall Transpiration and Free-stream Turbulence. Part II - Effects of Streamline Curvature and Spanwise Rotation," *Journal of Fluid Engineering*, Vol. 115, 1993, pp. 56–69.

[17]Schumann, U., "Realizability of Reynolds Stress Turbulence Models," *Physics of Fluid*, Vol. 20, No. 5, 1977, pp. 721–725.

[18]Speziale, C. G., Abid, R., and Durbin, P. A., "On the Realisability of Reynolds Stress Turbulence Closures," *Journal of Scientific Computing*, Vol. 9, No. 4, 1994, pp. 369–403.

[19]Tritton, D. J., "Stabilization and destabilization of turbulent shear flow in a rotating fluid," *Journal of Fluid Mechanics*, Vol. 241, 1992, pp. 503–523.

[20]Sviridenkov, A. A. and Yagodkin, V. I., "Flows in the Initial Sections of Channels with Permeable Walls," *Fluid Dynamics*, Vol. 11, 1976, pp. 43–48.

[21]Sabnis, J. S., Madabhushi, R. K., Gibeling, H. J., and Donald, H. M., "On the Use of $k - \epsilon$ Turbulence Model for Computation of Solid Rocket Internal Flows," AIAA Paper 89–2558, Jul. 1989, In 25th AIAA/ASME/SAE/ASEE Joint Propulsion Conference and Exhibit.

[22]Chaouat, B., "Computation using $k-\epsilon$ Model with Turbulent Mass Transfer in the Wall Region," 11^{th} *Symposium on Turbulence Shear Flows*, Vol. 2, 1997, pp. 2.71–2.76.

[23]Beddini, R. A., "Injection-Induced Flows in Porous-Walled Ducts," *AIAA Journal*, Vol. 11, No. 6, 1986, pp. 1766–1773.

[24]Yamada, K., Goto, M., and Ishikawa, N., "Simulative Study on the Erosive Burning of Solid Rocket Motors," *AIAA Journal*, Vol. 14, No. 9, 1976, pp. 1170–1176.

[25]R. Dunlap, P. G. W. and Hermsen, R. W., "Flowfield in the Combustion Chamber of a Solid Propellant Rocket Motor," *AIAA Journal*, Vol. 12, No. 10, 1974, pp. 1440–1443.

[26]Ramachandran, N., Heaman, J., and Smith, A., "An Experimental Study of the Fluid Mechanics Associated with Porous Walls," AIAA Paper 92–0769, Jan. 1992, In 30th Aerospace Sciences Meeting and Exhibit.

[27]Myong, H. and Kasagi, N., "A New Approach to the Improvement of $k-\epsilon$ Turbulence Model for Wall-Bounded Shear Flows," *JSME International Journal*, Vol. 33, No. 1, 1990, pp. 63–72.

List of Figure Captions

Figure 1: Schematic of fully-developed turbulent channel flow in a rotating frame.

Figure 2: (a) Mean velocity profile $\bar{u}_1/u_\tau$ in logarithmic coordinates; Δ: DNS; solid-line: RSM. (b)Root-mean square velocity fluctuations normalized by the wall shear velocity in global coordinates; Symbols: DNS data; lines: RSM; $(\widetilde{u_1''u_1''})^{1/2}/u_\tau$: Δ, solid-line; $(\widetilde{u_2''u_2''})^{1/2}/u_\tau$: $\triangleleft$, dashed-line; $(\widetilde{u_3''u_3''})^{1/2}/u_\tau$: $\triangleright$, dotted-line.

Figure 3: (a),(b) Mean velocity profile $\bar{u}_1/u_m$ in global coordinates; Δ: DNS; solid-line: RSM. (c),(d) Root-mean square velocity fluctuations normalized by the bulk velocity; Symbols: DNS data; lines: RSM; $(\widetilde{u_1''u_1''})^{1/2}/u_m$: Δ, solid-line; $(\widetilde{u_2''u_2''})^{1/2}/u_m$: $\triangleleft$, dashed-line; $(\widetilde{u_3''u_3''})^{1/2}/u_m$: $\triangleright$, dotted-line. (e),(f) Turbulent Reynolds shear stress normalized by the bulk velocity in global coordinates $\widetilde{u_1''u_2''}/u_m^2$; Δ: DNS; solid-line: RSM.

Figure 4: Variation with the rotation number $R_{ot} = \Omega\delta/u_m$ of the normalized cyclonic and anticyclonic friction velocities. Solid-line,$\triangleleft$,$\triangleright$: DNS results from Kristoffersen et al.;[2] dotted-line,$\triangle$,$\triangledown$: DNS results from Lamballais et al.;[3] dashed-line,$\square$,$\lozenge$: present RSM results.

Figure 5: Solution trajectories in fully developed rotating channel flow projected onto the second-invariant/third-invariant plane.

Figure 6: Schematic of channel flow with fluid injection.

Figure 7: (a)Streamlines and mean flow velocity field; $\sigma_s = 0.2$. (b) Mach number contours; $\Delta = 0.01$; $\sigma_s = 0.2$. (c),(d) Contours of turbulent Reynolds number $R_t = k^2/\nu\epsilon$; $\Delta = 110$; (c): $\sigma_s = 0.2$; $0 < R_t < 4000$. (d): $\sigma_s = 0.5$; $0 < R_t < 4200$.

Figure 8: Axial variations of turbulent coefficients for different values of the injection paramater σ_s. (a) Reynolds number R_τ; (b) coefficient α. Dot-dashed-line: $\sigma_s = 0.1$; dotted-line: $\sigma_s = 0.2$; dashed-line: $\sigma_s = 0.3$; long-dashed-line: $\sigma_s = 0.4$; solid-line: $\sigma_s = 0.5$.

Figure 9: (a) Mean dimensionless velocity profiles. (b) Root-mean square velocity fluctuations normalized by the bulk velocity $(\widetilde{u_1''u_1''})^{1/2}/u_m$. (c) $(\widetilde{u_2''u_2''})^{1/2}/u_m$. (d) $\widetilde{u_1''u_2''}/u_m^2$. $\sigma_s = 0.2$. Symbols: experimental data; lines: RSM. $x_1 = 22$ cm: $\triangleleft$, dotted-line; 40 cm: $+$, dashed-line; 57 cm: $\circ$, solid-line.

Figure 10: Root-mean square velocity fluctuations normalized by the bulk velocity $(\widetilde{u_2''u_2''})^{1/2}/u_m$. $\sigma_s = 0.2$. Symbols: experimental data; solid-line: RSM; dashed-line: $k - \epsilon$. (a) 35 cm: $\triangleright$; (b) 45 cm: $\square$

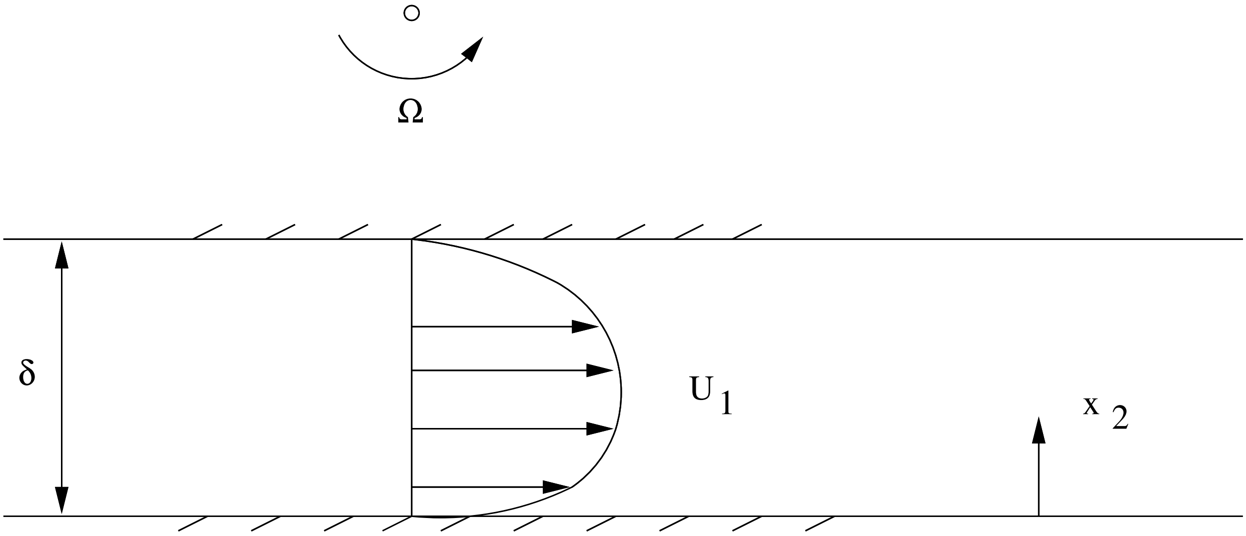

Ω
δ
U 1
x 2

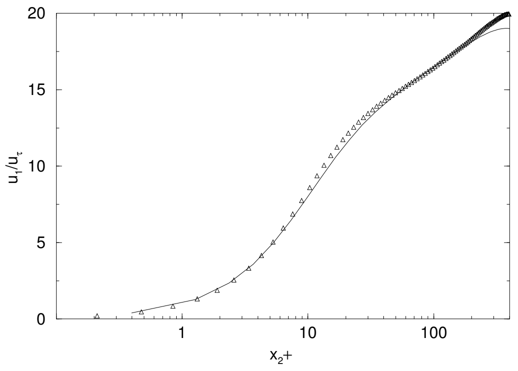

a) $R_\tau = 395$

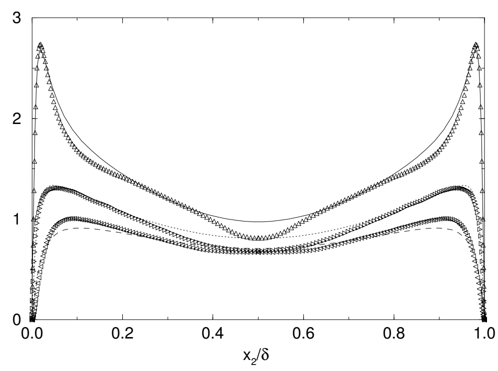

b) $R_\tau = 395$

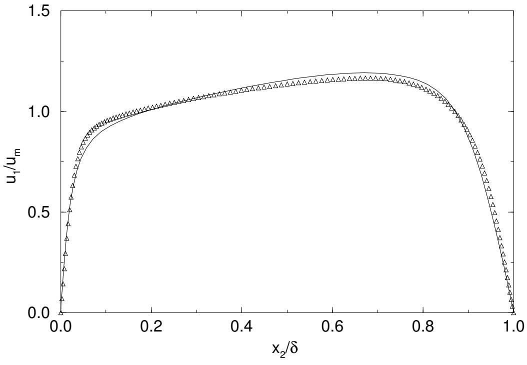

a) $R_\tau = 162$, $R_o = 18$

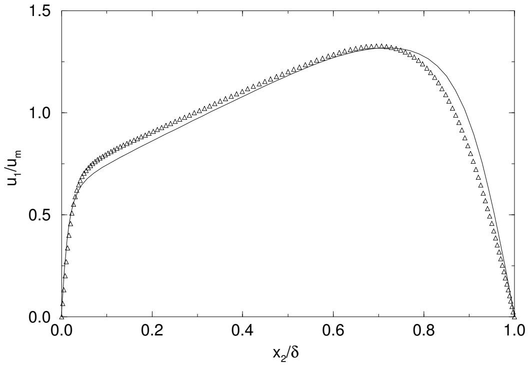

b) $R_\tau = 162$, $R_o = 6$

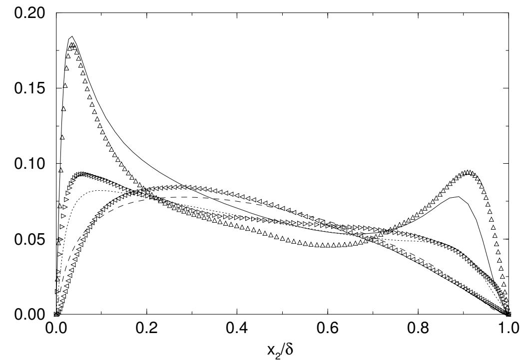

c) $R_\tau = 162$, $R_o = 18$

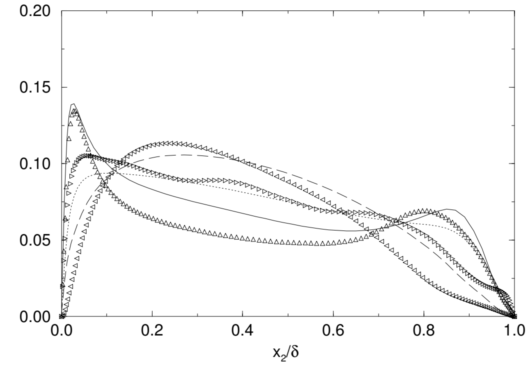

d) $R_\tau = 162$, $R_o = 6$

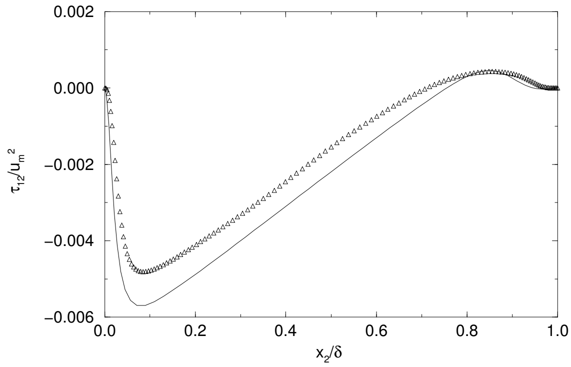

e) $R_\tau = 162$, $R_o = 18$

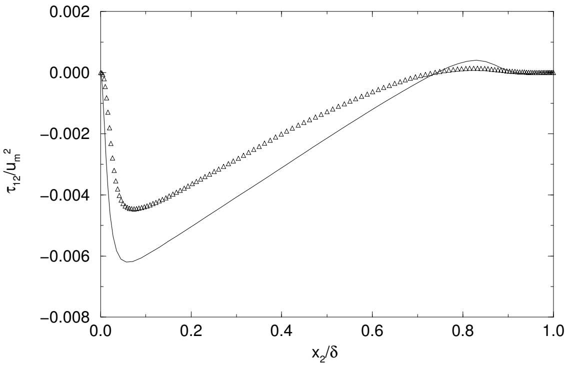

f) $R_\tau = 162$, $R_o = 6$

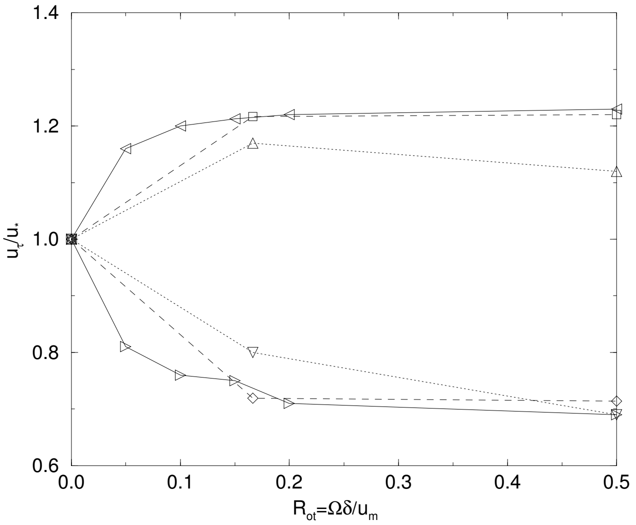
1.4
1.2
1.0
0.8
0.6
u_τ/u_*
0.0
0.1
0.2
0.3
0.4
0.5
$R_{ot}=\Omega\delta/u_m$

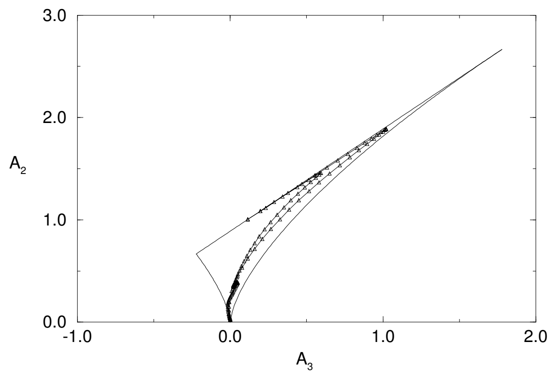

a) DNS

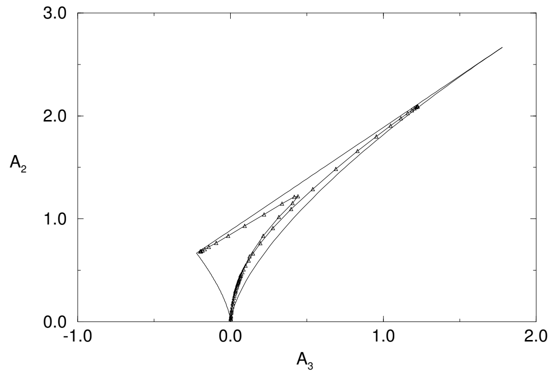

b) RSM

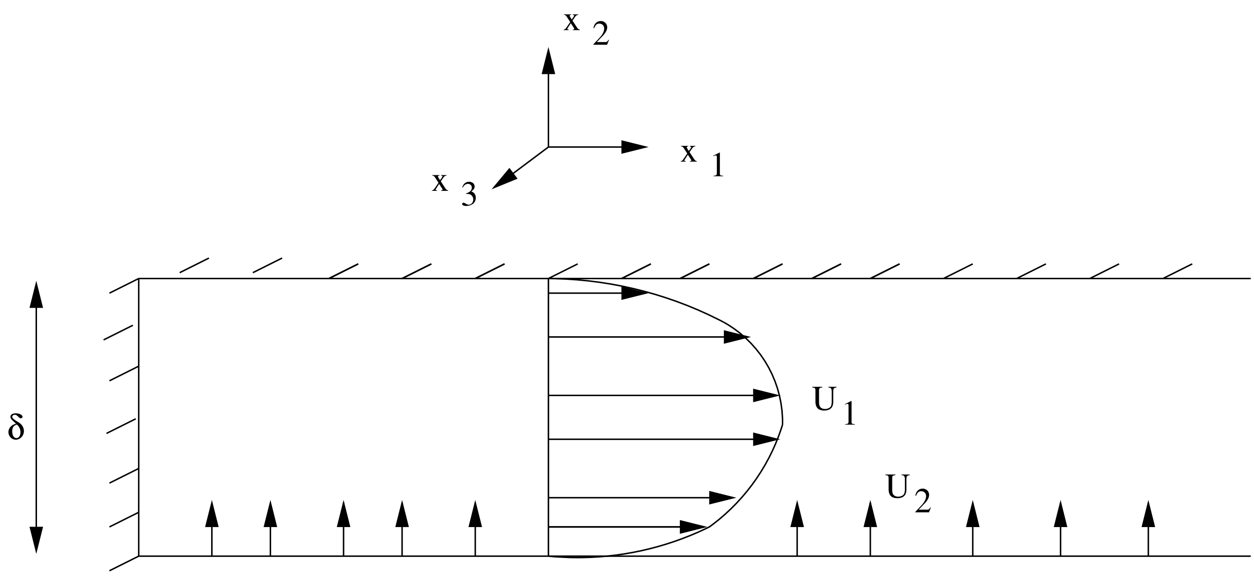
x 2
x 1
x 3
δ
U 1
U 2

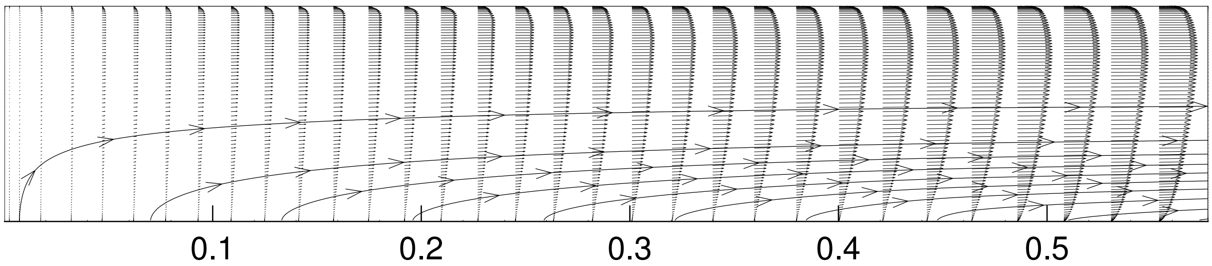

a)

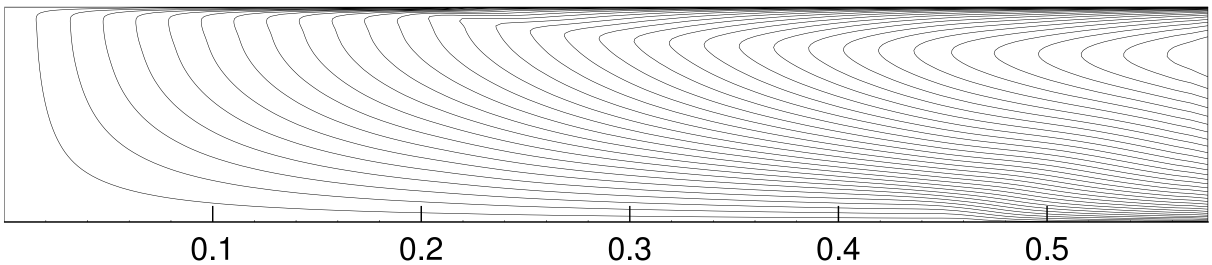

b)

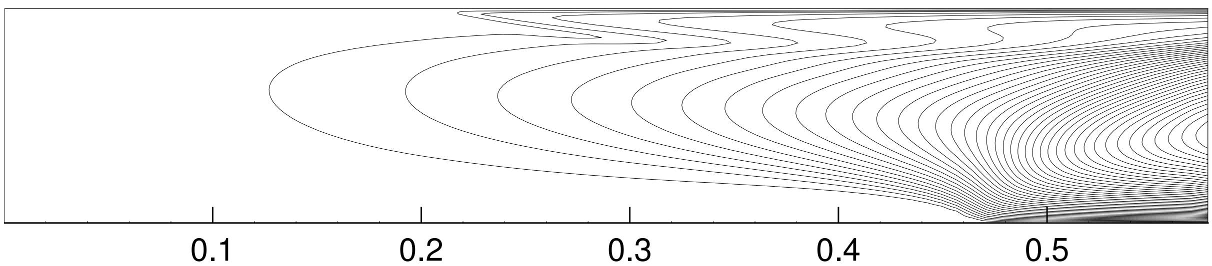

c)

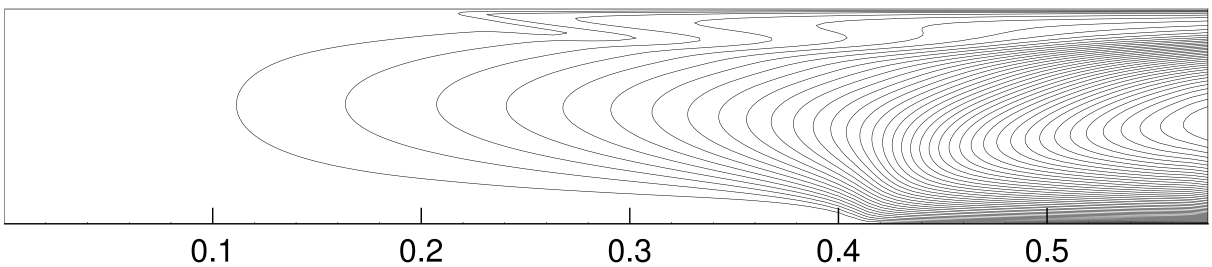

d)

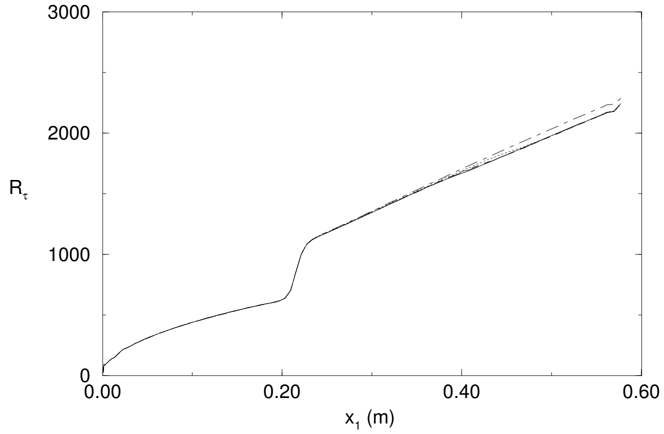
3000
2000
1000
0
R_τ
0.00
0.20
0.40
0.60
x_1 (m)

a)

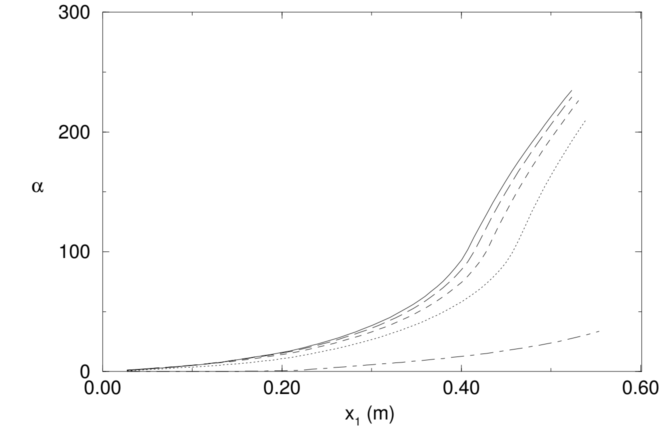
300
200
100
0
α
0.00
0.20
0.40
0.60
x_1 (m)

b)

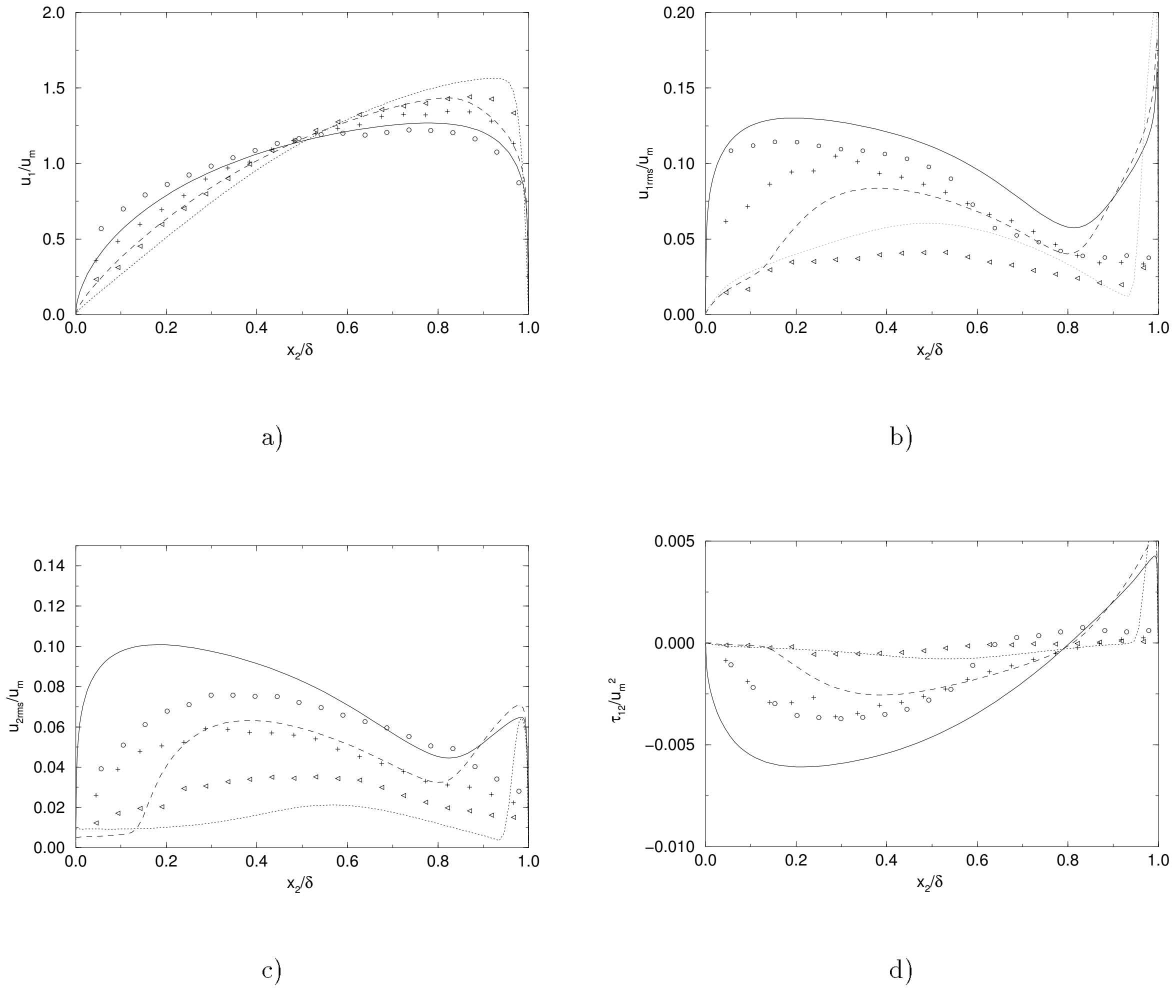

a) b) c) d)

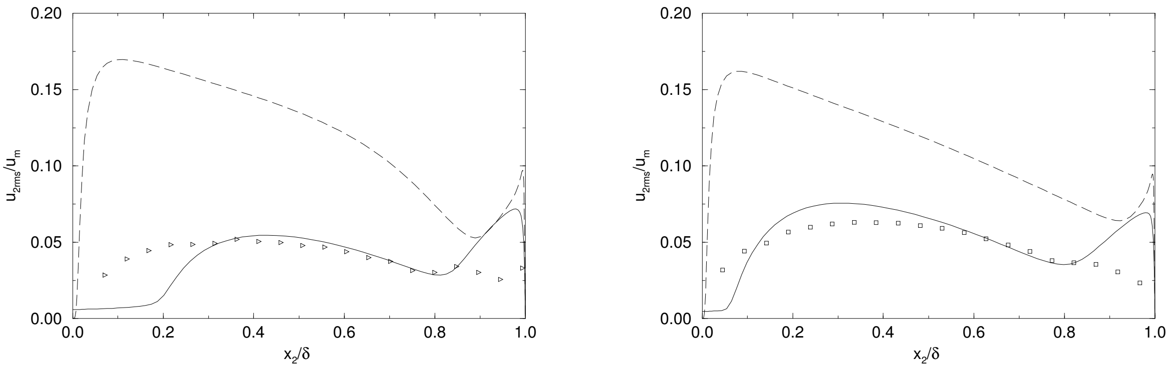
0.20
0.15
0.10
0.05
0.00
u2rms/um
0.0
0.2
0.4
0.6
0.8
1.0
x2/δ
0.20
0.15
0.10
0.05
0.00
u2rms/um
0.0
0.2
0.4
0.6
0.8
1.0
x2/δ

a) b)